

Communication

# The Facile Synthesis of Hollow CuS Microspheres Assembled from Nanosheets for Li-Ion Storage and Photocatalytic Applications

Yiyang Zhao, Yonghui Shao, Hao Chen, Xinwen Luo and Xiaodi Liu \*

College of Chemistry and Pharmaceutical Engineering, Nanyang Normal University, Nanyang 473061, China

\* Correspondence: 20122029@nynu.edu.cn; Tel.: +86-377-63513540

**Abstract:** Herein, well-defined hollow CuS microspheres assembled from nanosheets were successfully synthesized through a facile solvothermal method. Hollow CuS microspheres have an average diameter of 1.5  $\mu\text{m}$ ; moreover, the primary CuS nanosheets have an ultrathin thickness of about 10 nm and are bound by {0001} polar facets. When used as anodes for lithium-ion batteries (LIBs), hollow CuS microspheres exhibit excellent electrochemical properties, including a large discharge capacity (610.1  $\text{mAh g}^{-1}$  at 0.5 C), an excellent rate capability (207.6 and 143.4  $\text{mAh g}^{-1}$  at 1 and 5 C), and a superior cyclic stability (196.3  $\text{mAh g}^{-1}$  at 1 C after 500 cycles). When used as photocatalysts for Rhodamine B (RhB), hollow CuS microspheres can degrade more than 99% of the initial RhB within 21 min. These excellent Li-ion storage properties and photocatalytic performances are attributed to their unique hierarchical hollow structure.

**Keywords:** CuS; hollow microsphere; nanosheet; lithium-ion batteries; photocatalyst



**Citation:** Zhao, Y.; Shao, Y.; Chen, H.; Luo, X.; Liu, X. The Facile Synthesis of Hollow CuS Microspheres Assembled from Nanosheets for Li-Ion Storage and Photocatalytic Applications. *Nanomaterials* **2023**, *13*, 1505. <https://doi.org/10.3390/nano13091505>

Academic Editors: Henrich Frielinghaus and Christian M. Julien

Received: 20 March 2023

Revised: 13 April 2023

Accepted: 26 April 2023

Published: 28 April 2023



**Copyright:** © 2023 by the authors. Licensee MDPI, Basel, Switzerland. This article is an open access article distributed under the terms and conditions of the Creative Commons Attribution (CC BY) license (<https://creativecommons.org/licenses/by/4.0/>).

## 1. Introduction

Recently, with energy and environment issues becoming more and more prominent, developing high-performance electrochemical energy storage (EES) devices and high-efficiency pollution control technologies has attracted tremendous research attention [1,2]. For the former, lithium-ion batteries (LIBs) are extensively used as critical EES devices for portable electronic devices and electrified vehicles, and the exploration of effective anode materials may result in high-performance LIBs [3,4]. For the latter, photocatalytic treatment is a promising method for eliminating the organic and toxic pollutants in water, and photocatalysts are a key factor that affects the photocatalytic activity [5,6].

Until now, several advanced materials, such as CuS,  $\text{Fe}_2\text{O}_3$ ,  $\text{TiO}_2$ ,  $\text{Nb}_2\text{O}_5$ , and so on, have not only served as anodes for LIBs, but have also acted as photocatalysts for wastewater treatment [5,7–11]. Among them, CuS has received increasing interest due to its unique optical and electrical properties. When used as an anode for LIBs, CuS possesses exceptional qualities, including a high theoretical capacity (561  $\text{mAh g}^{-1}$ ), a good metal-like electronic conductivity ( $1 \times 10^{-3} \text{ S cm}^{-1}$ ), a special layered structure with large interlayer spacing, large abundant resources, and high safety [12,13]. However, as a kind of typical 2D material, CuS has a strong tendency to stack with each other [14]. Thus, the length of the charge transport paths would be increased and the electrochemically active area would be decreased, leading to a limited rate capability and cycle stability.

On the other hand, as a p-type semiconductor with a favorable bandgap (ca. 2.2 eV), CuS has received considerable attention for the treatment of toxic organic dyes [15,16]. Its photocatalytic property is closely related to the photogenerated electron–hole pairs of the photocatalyst, and so much effort has been focused on improving its photocatalytic performance by increasing the surface area, light absorptivity, and collection of charge carriers [8]. In this regard, the design of CuS for excellent Li-ion storage performance and photocatalytic activity is expected.

The construction of CuS nanomaterials is an efficient method for improving their physico-chemical properties, owing to their small size and large specific surface area [17,18]. Nevertheless, nanomaterials have a strong tendency to aggregate with each other due to their large surface energy, thus leading to poor performance. The construction of hierarchical micro/nanostructures assembled from nanoscale building blocks is an effective approach to prohibiting the agglomeration of nanomaterials; moreover, hierarchical structures possess special physical and chemical properties [18–21]. Among a wide range of hierarchical superstructures, hollow microspheres composed of nanosheets can supply a high surface area, low material density, good surface penetration, high charge transport rate, and good light absorptivity [8,22–24]. Thus, a hierarchical hollow microsphere is an ideal structure for obtaining excellent electrical and optical properties. Until now, several methods, including the templates sacrificial technique [25], Kirkendall effect [26], and precursor transformation [27], have been employed to prepare these hierarchical hollow microspheres. However, it still remains a challenge to explore facile and effective approaches to constructing well-defined hollow CuS microspheres.

Herein, nanosheet-assembled hollow CuS microspheres were prepared by a facile solvothermal method without using templates. By simply changing the volume ratio of deionized water to glycerol, uniform hollow microspheres can be obtained. Their hollow structure is beneficial for the penetration of electrolyte into electrodes and supplies extra active sites for the storage of  $\text{Li}^+$  ions. Moreover, the special hollow structure significantly enhances the light absorption capabilities. Accordingly, hollow CuS microspheres possess excellent Li-ion storage properties and photocatalytic activity.

## 2. Materials and Methods

### 2.1. Synthesis of Hollow CuS Microspheres

All the chemicals were purchased from Shanghai Aladdin Bio-Chem Technology Co., Ltd. (Shanghai, China). In the typical synthesis, 5 mmol  $\text{CuSO}_4 \cdot 5\text{H}_2\text{O}$  and 10 mmol  $\text{CH}_3\text{CSNH}_2$  (TAA) were added into 15 mL of a deionized water–glycerol solvent (with a volume ratio of deionized water to glycerol,  $R_{w/g}$ , of 5:1). After being stirred for 15 min, the solution was moved into a Teflon-lined autoclave (30 mL) and maintained at 150 °C for 9 h. After the samples were centrifuged, washed, and dried, hollow CuS microspheres (denoted by S-1) were obtained. In addition, to inspect the influence of the solvent on the morphology of the products, the same procedure as that for the synthesis of S-1 was used for the fabrication of S-2 and S-3, except that the  $R_{w/g}$  values were 1:0 and 2:1, respectively.

### 2.2. Materials Characterization

The crystal structures of the products were analyzed using a Rigaku D/max 2500V/PC X-ray diffractometer (XRD, Rigaku Corporation, Tokyo, Japan) using  $\text{Cu K}\alpha$  as radiation. The morphologies and nanostructures of the samples were researched using SU8010 field-emission scanning electron microscopy (FESEM, Hitachi, Ltd., Tokyo, Japan) and JEM-2100F transmission electron microscopy (TEM, JEOL Ltd., Tokyo, Japan). The Brunauer–Emmett–Teller (BET) special surface area of the sample was researched using the  $\text{N}_2$  adsorption–desorption isotherms on a Micromeritics Autosorb-iQ apparatus (Quantachrome Inc., Florida, FL, USA). The X-ray photoelectron spectra (XPS, Thermo Fisher Scientific Inc., Massachusetts, MA, USA) were researched using a Thermo ESCALAB 250XI electron spectrometer.

### 2.3. Electrochemical Measurement

S-1, acetylene black, and polyvinylidene fluoride with a ratio of 70:20:10 wt% were mixed into N-methyl-2-pyrrolidone. The slurry was uniformly coated on Cu foils and then dried in vacuum at 120 °C for 12 h. Subsequently, the electrodes were assembled into CR2025 coin-type cells in an Argon-filled glove box. Li was served as the counter and reference electrode. The electrolyte was 1 mol·L<sup>-1</sup>  $\text{LiPF}_6$  in ethylene carbonate, ethyl methyl carbonate, and diethyl carbonate (1:1:1 vol%). Cyclic voltammetry (CV) measurements were

carried out on a CHI660D Electrochemical Workstation (Shanghai Chenhua Instrument Ltd., Shanghai, China).

#### 2.4. Photocatalytic Test

The photocatalytic activities of S-1 and S-2 were researched using the photodegradation of Rhodamine B (RhB), using a 500 W Xe lamp equipped with a UV cut-off filter ( $\lambda > 420$  nm) as the irradiation source. In the typical photocatalytic experiment, 10 mg of the photocatalyst was added into 100 mL of a RhB dye solution (10 mg/L). Prior to irradiation, the obtained suspension was magnetically stirred for 30 min in the dark to reach an adsorption–desorption equilibrium. In the following photocatalytic reaction, 4 mL of the suspension was collected at a given time interval and centrifuged (10,000 rpm, 5 min) to remove the photocatalyst. The contents of RhB were tested by detecting the values of feature absorbance of 553 nm on a Lambda 650 s UV-Vis spectrophotometer (Perkin Elmer Instruments Inc., Massachusetts, MA, USA).

### 3. Results

#### 3.1. Structure Characterization

The composition, morphology, and nanostructure of S-1 were researched using XRD, SEM, TEM, and HRTEM. Figure 1a displays the XRD pattern of S-1. Obviously, the positions and intensities of all the diffraction peaks are in good agreement with the hexagonal CuS phase (JCPDS No. 06-0464). The strong peaks with  $2\theta$  values of  $29.3^\circ$ ,  $31.8^\circ$ ,  $32.9^\circ$ , and  $47.9^\circ$  correspond to the (102), (103), (006), and (110) facets of the hexagonal CuS, respectively. No other peaks for impurities such as  $\text{Cu}_2\text{S}$  or CuO are observed, indicating that S-1 is highly pure. In addition, the sharp diffraction peaks reveal the good crystalline nature of S-1. From the FESEM image (Figure 1b), it can be observed that the products are well-defined microspheres with an average diameter of about 1.5  $\mu\text{m}$ . As shown in the high-magnification FESEM image (inset of Figure 1b), the microspheres are composed of small hexagonal nanosheets with an edge length of about 30 nm and a thickness of about 10 nm. As indicated by the red arrows in Figure 1b, the microspheres possess a hollow structure.

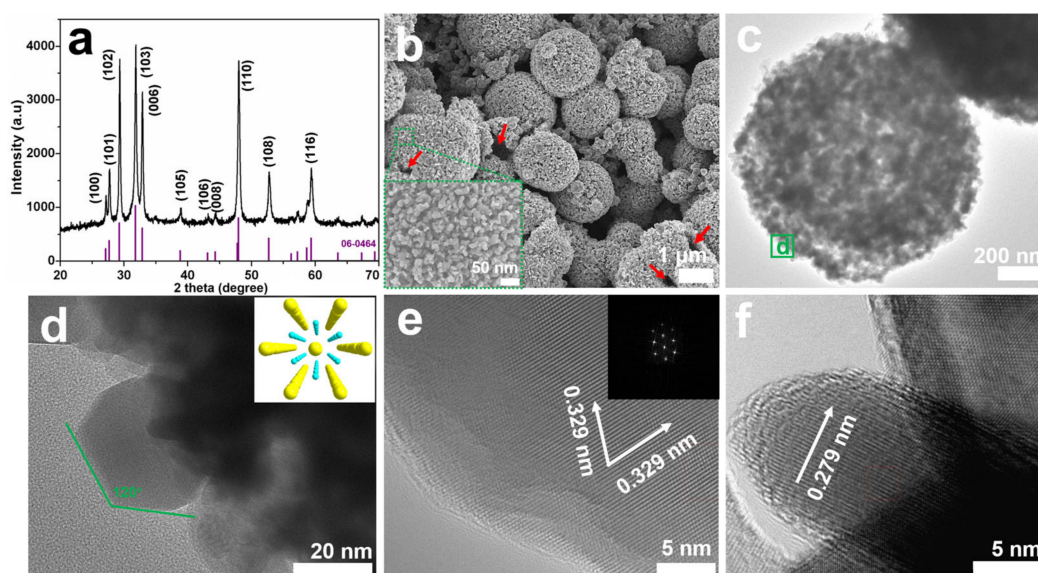


**Figure 1.** (a) XRD pattern of S-1, and the purple lines are the standard XRD reflections of hexagonal CuS; (b) FESEM image and (c) TEM image of S-1; (d) high-magnification TEM image of S-1 originating from the green square in (c), the inset is the atomic arrangement of hexagonal CuS viewed along the  $c$ -axis (● Cu, ● S); (e) HRTEM image of a primary nanosheet, the inset is the corresponding FFT pattern from the [001] direction; and (f) HRTEM image of a nanosheet standing perpendicular to the substrate.

In the corresponding TEM image (Figure 1c), the contrast between the dark edge and light center further affirms the hollow interior void of S-1 [22]; furthermore, the high-magnification TEM image (Figure 1d, taken from the green square d in Figure 1c) clearly points out that these primary nanosheets have symmetrical hexagonal shapes. The HRTEM image taken of the typical hexagonal nanosheet (Figure 1e) exhibits continuous lattice fringes, further showing the good crystallization of S-1. Two clear lattice fringes have similar lattice fringes of ca. 0.329 nm, corresponding to the *d*-spacing of the (100) and (010) facets. Additionally, it should be mentioned that the hexagonal symmetry spots in the corresponding fast Fourier transform (FFT) pattern (inset of Figure 1e) are consistent with the atomic arrangement of the hexagonal CuS along the *c*-axis (inset of Figure 1d). Furthermore, the (006) plane with a lattice spacing of ca. 0.279 nm can be clearly seen from the HRTEM image of a nanosheet standing on the substrate (Figure 1f). Therefore, it can be deduced that these sheet-like building blocks are mainly bound by {0001} polar facets [28]. Owing to its hierarchical hollow microstructure, S-1 has a large specific surface area of 50.8 m<sup>2</sup> g<sup>-1</sup> (Figure S1), which is beneficial for improving Li-ion storage properties and photocatalytic performance.

XPS was further used to inspect the surface composition and chemical state of S-1. The signals, including the Cu, S, C, and O elements, can be detected from the wide-scan XPS survey of S-1 (Figure S2). The O1s signal at 532.1 eV is relatively weak, revealing the adsorption of oxygen on the surface of S-1 [29]. Moreover, the Auger line of Cu (Cu LMM) appears at 569.1 eV, corresponding to a kinetic energy of 917.5 eV, indicating that the Cu element in CuS is presented in the form of Cu<sup>2+</sup> [30]. Figure 2a,b are the high-resolution Cu 2p and S 2p XPS spectra, respectively. In Figure 2a, the two main peaks at around 932.5 and 952.4 eV can be ascribed to the Cu 2p<sub>3/2</sub> and Cu 2p<sub>1/2</sub> of the Cu<sup>2+</sup> in CuS, respectively, and these values are for the Cu<sup>2+</sup> oxidation state in CuS [15,31]. Meanwhile, as shown in Figure 2b, the S 2p core-level spectrum of S-1 can be fitted to three peaks at 161.9, 162.8, and 163.9 eV. The first two peaks can be assigned to the Cu-S bond and the last one is attributed to the S-S bond [12]. According to the XPS results, the atomic ratio of Cu to S is about 47.7:52.3. The superfluous S may be caused by the excess amount of TAA.

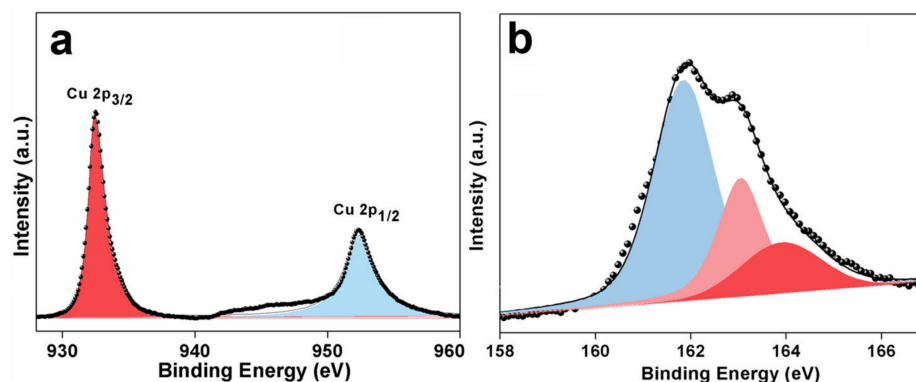
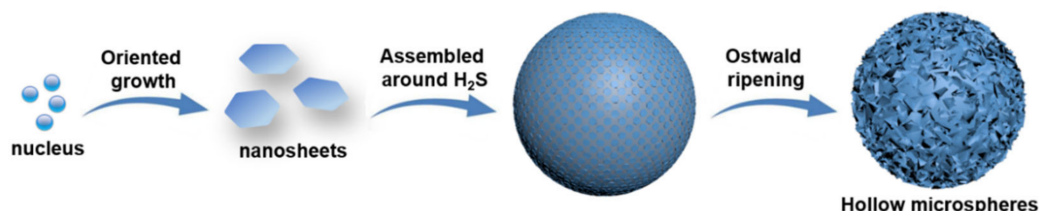


Figure 2. (a) Cu 2p, and (b) S 2p XPS spectra of S-1.

### 3.2. Formation Mechanism

During the synthesis, the Cu<sup>2+</sup> ions first react with TAA to form [Cu(TAA)<sub>2</sub>]<sup>2+</sup> complex ions (Cu<sup>2+</sup> + 2TAA → [Cu(TAA)<sub>2</sub>]<sup>2+</sup>) and then these [Cu(TAA)<sub>2</sub>]<sup>2+</sup> ions are converted into CuS nuclei and H<sub>2</sub>S gas ([Cu(TAA)<sub>2</sub>]<sup>2+</sup> + 4H<sub>2</sub>O → CuS↓ + 2H<sup>+</sup> + 2CH<sub>3</sub>COONH<sub>4</sub> + H<sub>2</sub>S↑). It is known that the growth orientations of crystals are closely related to their intrinsic crystal structures [32]. According to the XRD result (Figure 1a), the crystal structure of hexagonal CuS belongs to the P63/mmc space group, with lattice parameters of *a* = *b* = 3.793 Å and *c* = 16.346 Å. In the crystal structure of hexagonal CuS, two kinds of close-packed atom layers ([CuS<sub>3</sub>] and [Cu<sub>3</sub>S]) are alternatively arranged along the [001] direction. Specifically, in the [CuS<sub>3</sub>] layer, each Cu atom is coordinated by four S atoms to form a tetrahedron, whereas each Cu atom in the [Cu<sub>3</sub>S] layer is coordinated by three

S atoms in a triangle [28]. Owing to this anisotropic characteristic, CuS nuclei prefer to grow in the *ab* planes rather than along the *c*-axis, resulting in the generation of hexagonal sheet-like building blocks [33]. During the following growth process, to minimize the surface energies, the primary CuS nanosheets tend to assemble around the interfaces of H<sub>2</sub>S gas bubbles [34,35]. Finally, a hierarchical hollow structure can be formed. The possible formation mechanism of S-1 is illustrated in Figure 3.



**Figure 3.** Illustration of the possible formation mechanism of S-1.

In the synthetic system, it is deduced that glycerol content plays an important role in the formation of S-1. Glycerol has a considerably higher viscosity than water (243 vs. 3 mPa s), so the primary CuS nanosheets have sufficient time to search for the low-energy configuration interface and assemble into a well-defined hollow microstructure in the deionized water–glycerol solvent [36]. Controlled experiments with different solvent components are conducted to verify the influence of the solvent on the structures of the products. As shown in Figure S3, the products prepared with different solvents are CuS with high purity. As the solvent contains only 15 mL of deionized water, the products (S-2) are composed of hollow microspheres and irregular aggregates (Figure 4a). Owing to the low viscosity of water, the primary nanosheets can be quickly aggregated with each other. Finally, some nanosheets are aggregated into hollow microspheres with a thick shell, and the others are assembled into irregular aggregates. As the content of the glycerol is increased to 5 mL (S-3), the solvent has an increased viscosity, which is not only averse to the anisotropic growth of hexagonal building blocks, but also hinders the formation of uniform microstructures. Hence, the products are mainly CuS messy aggregates (Figure 4b). The detailed experimental conditions and corresponding morphologies are summarized in Table S1.

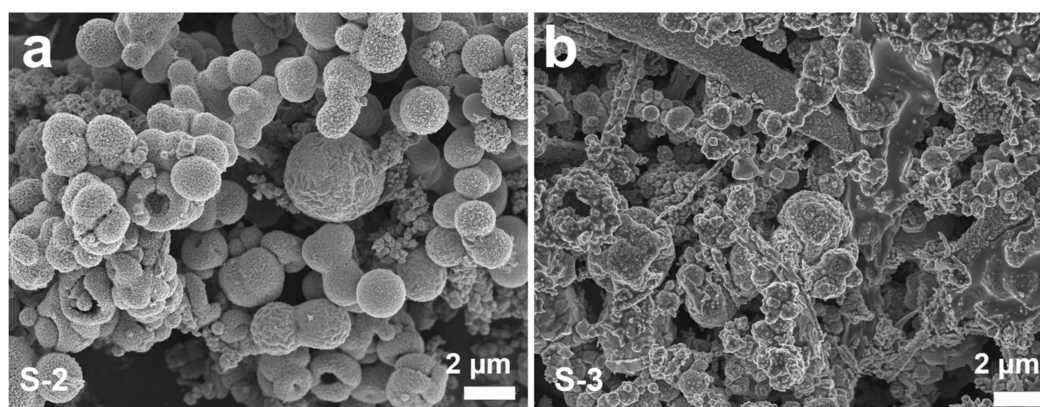


**Figure 4.** FESEM images of CuS prepared at different solvents with the other reaction parameters unchanged: (a) 15 mL deionized water (S-2); and (b) 10 mL deionized water and 5 mL glycerol (S-3).

### 3.3. Li-Ion Storage Properties

The cyclic voltammogram (CV) curve of S-1 was tested at a scan rate of 0.1 mV s<sup>−1</sup> over a voltage range of 0.01–3.0 V (vs. Li<sup>+</sup>/Li), and the result of this is shown in Figure S4. Similar to other papers [37,38], the reduction peak in the discharge process represents the conversion of Li<sub>x</sub>CuS (CuS + xLi<sup>+</sup> + xe<sup>−</sup> → Li<sub>x</sub>CuS) and the oxidation peaks

in the charge process are associated with the formation of CuS. The Li-ion storage properties of S-1 were researched via the galvanostatic discharge–charge method. Figure 5a shows the first charge–discharge curves of S-1 in the voltage range of 0.01–3.0 V (vs.  $\text{Li}^+/\text{Li}$ ) at different current densities. As the current densities are 0.5, 1, 2, and 5 C, the first discharge capacities are 610.1, 230.7, 194.9, and 158.9  $\text{mAh g}^{-1}$ , respectively. The rate capability of S-1 was studied using a progressive discharge and charge from 0.5, 1 to 2, and 5 C for 10 cycles at each current density. As shown in Figure 5b, the anode exhibits excellent rate capacities of 230.6 to 207.6, 170.2, and 143.4  $\text{mAh g}^{-1}$  at 0.5, 1, 2, and 5 C, respectively. Furthermore, the discharge capacity returns to 192.3  $\text{mAh g}^{-1}$  as the current density is reduced to 1 C. These results indicate that the anode has an excellent rate performance and good structural stability at a high current density. The cyclic stability of S-1 was also investigated. The anode was first activated at a low current rate of 0.5 C for 10 cycles, and then the anode was repeatedly charged and discharged at 1 C. As shown in Figure 5c, S-1 exhibits a high reversible capacity of 196.3  $\text{mAh g}^{-1}$  after 500 cycles, keeping a capacity retention of 88.2% compared to the first cycle. Additionally, compared to other copper-sulfide-based anodes [39–44], S-1 shows comparable Li-ion storage properties (Table S2).

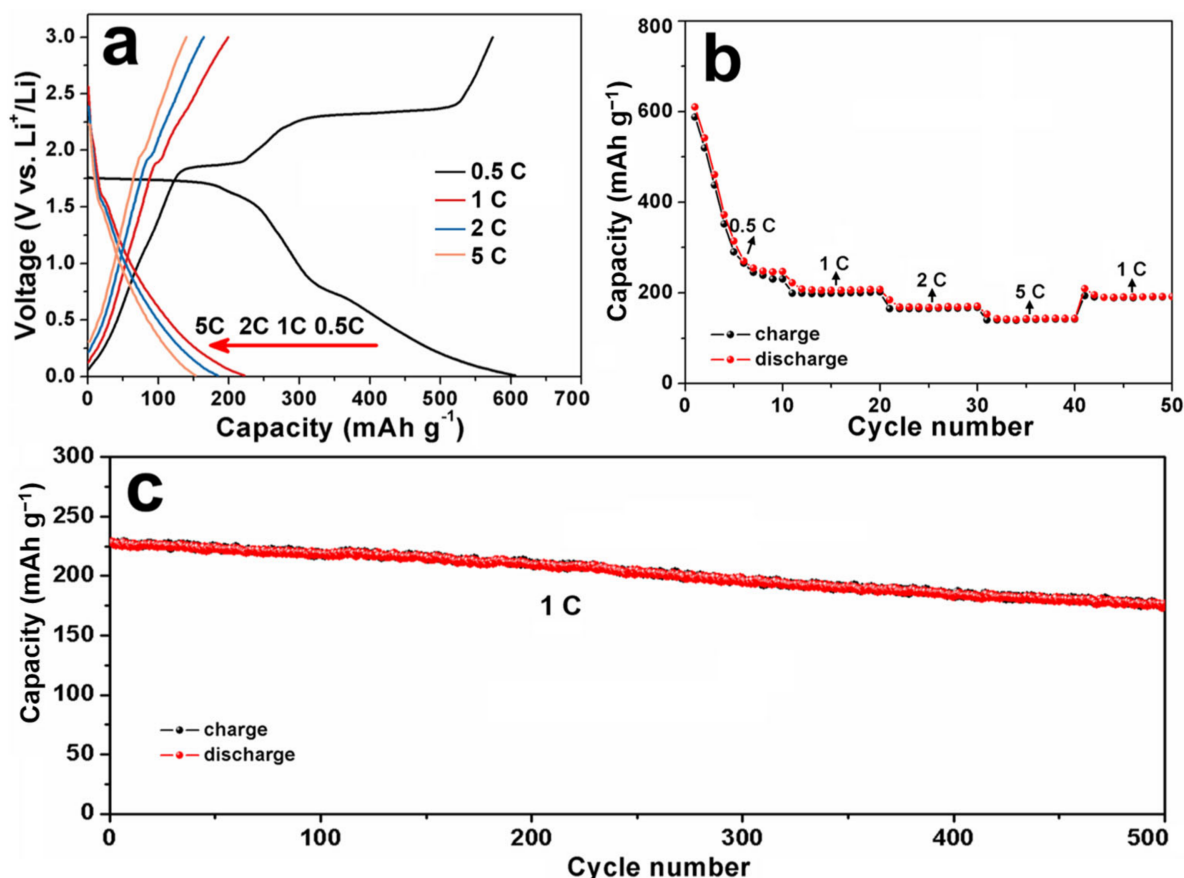


**Figure 5.** (a) The 1st discharge–charge curves of S-1 at different current densities; (b) rate capability; and (c) cycling performance of S-1.

Such results indicate that S-1 possesses excellent  $\text{Li}^+$  storage properties, which may be attributed to its unique structure. At first, its hierarchical hollow structure is beneficial for the penetration of electrolyte into electrode and it can supply extra active sites for the storage of  $\text{Li}^+$  ions. Thus, S-1 has a high discharge capacity [22,45]. Secondly, it is known that the time for the  $\text{Li}^+/\text{e}^-$  diffusion in the electrode is proportional to the diffusion length. The primary CuS nanosheets have a thin thickness (ca. 10 nm), so the transfer rate of  $\text{Li}^+$  and  $\text{e}^-$  can be effectively enhanced, resulting in a good rate capacity [20,46,47]. Thirdly, the

unique architecture of S-1 maintains the mechanical stability of the electrode during the discharge and charge processes, leading to an obvious improvement in its cycling stability.

### 3.4. Photocatalytic Performance

S-1 can be used as a photocatalyst for the degradation of organic dyes (e.g., RhB and MB) due to its unique hierarchical hollow structure. The photocatalytic performance of S-1 was tested by the photocatalytic degradation of RhB under visible light irradiation. As a comparison, S-2 was also tested under the same conditions. In the photocatalytic process [15,48], under the irradiation of visible light, CuS yields a pair of electrons ( $e^-$ ) and holes ( $h^+$ ) ( $CuS + h\nu \rightarrow e^- + h^+$ ). Then, the as-formed electrons leap into the bottom of the conduction band (CB) and react with  $O_2$  on the surface of the photocatalyst to form a superoxide radical ( $e^- + O_2 \rightarrow \cdot O_2^-$ ). In addition, the holes stay at the top of the valence band (VB) and react with  $H_2O$  to generate hydroxyl radicals ( $h^+ + H_2O \rightarrow \cdot OH + H^+$ ). Finally, the active substances ( $O_2^-$  and  $\cdot OH$ ) can oxidize RhB into smaller molecules ( $CO_2$ ,  $H_2O$ , etc.).

Figure 6a,b display the time-dependent absorption spectra of RhB aqueous solutions containing S-1 and S-2, respectively. With an increase in the irradiation time, the maximum absorption of RhB at 550 nm decreases, suggesting its decomposition. Figure 6c represents the photodegradation rates of the RhB aqueous solutions by using S-1 and S-2 as photocatalysts. Clearly, S-1 degrades more than 99% of the initial RhB within 21 min, whereas with S-2, only 68.3% of the RhB is decomposed after 20 min of irradiation, and 90.5% of the RhB can be decomposed after 40 min. Thus, S-1 exhibits stronger photocatalytic activity than S-2. Compared to some other metal sulfides [15,48–53], S-1 also exhibits an excellent photocatalytic performance (Table S3). Furthermore, it has been reported that copper sulfide photocatalysts suffer from photocorrosion under light irradiation, in which  $S^{2-}$  can be oxidized by  $h^+$  into  $S^0$  or  $SO_4^{2-}$ , thus decreasing the photocatalytic activity [54,55]. Accordingly, the recycled photocatalytic test was carried out to research the stability of S-1 (Figure S5). It can be found that the degradation rate of S-1 slightly decreases by 2.1% after eight cycles, suggesting that S-1 has a good cycling stability.

It is deduced that the outstanding degradation efficiency of S-1 stems from the following reasons. Firstly, S-1 has a large specific surface area, so it conveniently absorbs more photons and produces plenty of electron–hole pairs [56]. Secondly, as shown in Figure 6d, the hollow microspheres can reflect the incident light between the inner voids and shells of S-1, enhancing its light absorption capabilities [57,58]. Thirdly, it is known that the  $e^-/h^+$  recombination problem significantly affects the photocatalytic performance of photocatalysts. As for S-1, the ultrathin thickness of the primary nanosheets provides a short distance for the  $e^-$  transfer from the interior to the surface; moreover, the charge transfer is facilitated by the high crystallinity of the nanosheets. Hence, the  $h^+/e^-$  recombination in the bulk is suppressed and the photocatalytic performance of S-1 is enhanced accordingly [54,59]. Fourthly, the exposed facet also plays an important part in the photocatalytic properties of S-1 [60,61]. According to the HRTEM results, the flat surfaces of the primary nanosheets are exposed by the {0001} facets, while the lateral surfaces are exposed by the {10-10} facets. The self-constructed {0001}/{10-10} facet junctions in the CuS nanosheets can accelerate the charge carriers' separation and transfer [61]. Thus, the recombination of  $h^+$  and  $e^-$  is effectively prevented, endowing S-1 with a good photocatalytic activity and stability for organic pollutant degradation.

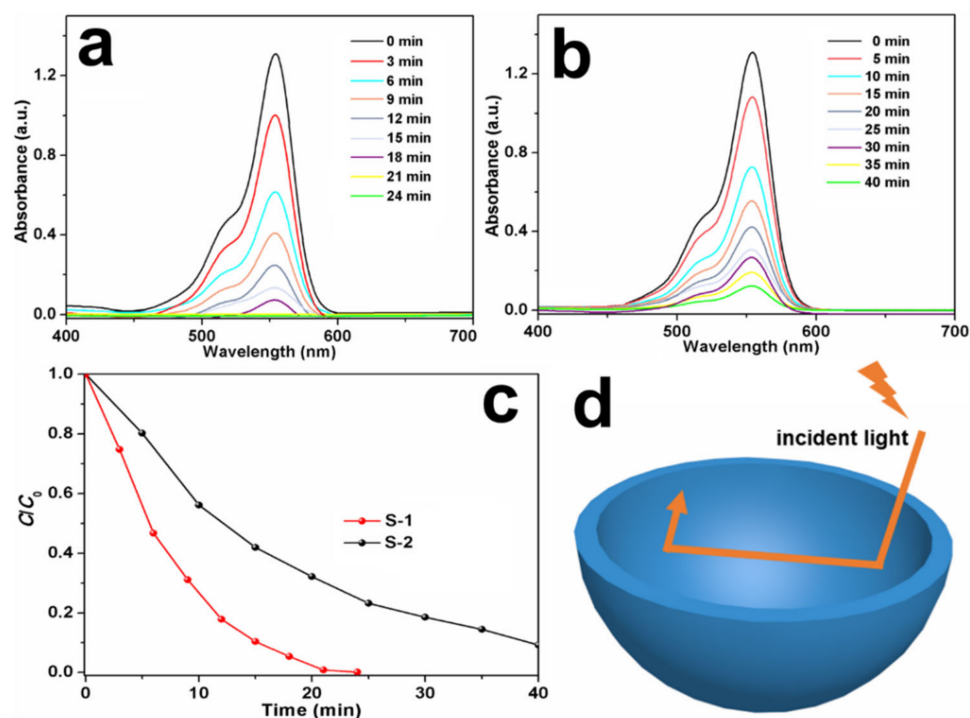


**Figure 6.** Time-dependent absorption spectra of RhB solutions in the presence of (a) S-1 and (b) S-2; (c) photodegradation rate of RhB solution by using S-1 and S-2 as photocatalysts; and (d) schematic illustration of the improved photocatalytic activity of S-1.

#### 4. Conclusions

In summary, we report the solvothermal syntheses, formation mechanisms, Li-ion storage properties, and photocatalytic performances of hollow CuS microspheres. Owing to the synergistic effects of their hollow structures, ultrathin nanosheets, special exposed facets, and hierarchical superstructures, hollow CuS microspheres have improved electrochemical and photocatalytic properties. At 0.5 C, hollow CuS microspheres exhibit a high discharge capacity of  $610.1 \text{ mAh g}^{-1}$  and they can retain a high capacity of  $143.4 \text{ mAh g}^{-1}$  even at 5 C. In addition, after 500 cycles at 1 C, they exhibit a high discharge capacity of  $196.3 \text{ mAh g}^{-1}$ . On the other hand, hollow CuS microspheres degrade more than 99% of RhB within 21 min. Hence, hollow CuS microspheres show potential applications as anodic material for LIBs and photocatalysts for the treatment of organic dyes.

**Supplementary Materials:** The following supporting information can be downloaded at: <https://www.mdpi.com/article/10.3390/nano13091505/s1>, Figure S1:  $\text{N}_2$  adsorption-desorption isotherm of S-1; Figure S2: Wide-scan XPS survey of S-1; Figure S3: XRD patterns of S-2 and S-3; Figure S4: CV curve of S-1 at a scan rate of  $0.1 \text{ mV s}^{-1}$ ; Figure S5: The photocatalytic cycling stability of S-1 for the degradation of RhB; Table S1: The detailed experimental conditions and corresponding morphologies of samples; Table S2: The comparison of the electrochemical performance of S-1 and other previously reported copper sulfides-based anodes for LIBs; Table S3: The comparison of the photocatalytic performance of S-1 and other previously reported metal sulfides for the degradation of organic dyes.

**Author Contributions:** Writing—original draft, Y.Z.; writing—review and editing, X.L. (Xiaodi Liu); methodology, X.L. (Xinwei Luo) and Y.S.; investigation Y.S. and H.C. All authors have read and agreed to the published version of the manuscript.

**Funding:** This research was funded by the National Natural Science Foundation of China, grant numbers 51802163 and 21501101, and the Natural Science Foundation of Henan Province of China, grant number 222300420252.

**Data Availability Statement:** Data sharing is not applicable to this article.

**Conflicts of Interest:** The authors declare no conflict of interest.

## References

1. Wei, C.; Chen, S.; Yu, C.; Wang, R.; Luo, Q.; Chen, S.; Wu, Z.; Liu, C.; Cheng, S.; Xia, J. Achieving high-performance  $\text{Li}_{6.5}\text{Sb}_{0.5}\text{Ge}_{0.5}\text{S}_5\text{I}$ -based all-solid-state lithium batteries. *Appl. Mater. Today* **2023**, *31*, 101770. [[CrossRef](#)]
2. Orimolade, B.O.; Idris, A.O.; Feleni, U.; Mamba, B. Recent advances in degradation of pharmaceuticals using  $\text{Bi}_2\text{WO}_6$  mediated photocatalysis—a comprehensive review. *Environ. Pollut.* **2021**, *289*, 117891. [[CrossRef](#)]
3. Golmohammadzadeh, R.; Faraji, F.; Jong, B.; Pozo-Gonzalo, C.; Banerjee, P.C. Current challenges and future opportunities toward recycling of spent lithium-ion batteries. *Renew. Sustain. Energy Rev.* **2022**, *159*, 112202. [[CrossRef](#)]
4. Lee, W.W.; Lee, J.M. Novel synthesis of high performance anode materials for lithium-ion batteries (LIBs). *J. Mater. Chem. A* **2014**, *2*, 1589–1626. [[CrossRef](#)]
5. Zhao, L.; Zhou, L.; Sun, C.; Gu, Y.; Wen, W.; Fang, X. Rose-like CuS microflowers and their enhanced visible-light photocatalytic performance. *CrystEngComm* **2018**, *20*, 6529–6537. [[CrossRef](#)]
6. Bell, J.D.; Murphy, J.A. Recent advances in visible light-activated radical coupling reactions triggered by (i) ruthenium, (ii) iridium and (iii) organic photoredox agents. *Chem. Soc. Rev.* **2021**, *50*, 9540–9685. [[CrossRef](#)] [[PubMed](#)]
7. Ding, C.; Su, D.; Ma, W.; Zhao, Y.; Yan, D.; Li, J.; Jin, H. Design of hierarchical CuS/graphene architectures with enhanced lithium storage capability. *Appl. Surf. Sci.* **2017**, *403*, 1–8. [[CrossRef](#)]
8. Zhu, J.; Yin, Z.; Yang, D.; Sun, T.; Yu, H.; Hoster, H.E.; Hng, H.H.; Zhang, H.; Yan, Q. Hierarchical hollow spheres composed of ultrathin  $\text{Fe}_2\text{O}_3$  nanosheets for lithium storage and photocatalytic water oxidation. *Energy Environ. Sci.* **2013**, *6*, 987–993. [[CrossRef](#)]
9. Xiao, S.; Lu, Y.; Li, X.; Xiao, B.Y.; Wu, L.; Song, J.P.; Xiao, Y.X.; Wu, S.M.; Wang, Y.; Chang, G.G.; et al. Hierarchically dual-mesoporous  $\text{TiO}_2$  microspheres for enhanced photocatalytic properties and lithium storage. *Chem. Eur. J.* **2018**, *24*, 13246–13252. [[CrossRef](#)]
10. Du, L.; Long, Z.; Wen, H.; Ge, W.; Zhou, Y.; Wang, J. (ionic liquid)-derived morphology control of  $\text{Nb}_2\text{O}_5$  materials and their photocatalytic properties. *CrystEngComm* **2014**, *16*, 9096–9103. [[CrossRef](#)]
11. Liu, X.; Liu, G.; Liu, Y.; Sun, R.; Ma, J.; Guo, J.; Hu, M. Urchin-like hierarchical H- $\text{Nb}_2\text{O}_5$  microspheres: Synthesis, formation mechanism and their applications in lithium ion batteries. *Dalton Trans.* **2017**, *46*, 10935–10940. [[CrossRef](#)]
12. An, C.; Ni, Y.; Wang, Z.; Li, X.; Liu, X. Facile fabrication of CuS micro-flower as high durable sodium-ion battery anode. *Inorg. Chem. Front.* **2018**, *5*, 1045–1052. [[CrossRef](#)]
13. Zhao, Y.; Wang, L.P.; Sougrati, M.T.; Feng, Z.; Leconte, Y.; Fisher, A.; Srinivasan, M.; Xu, Z. A review on design strategies for carbon based metal oxides and sulfides nanocomposites for high performance Li and Na ion battery anodes. *Adv. Energy Mater.* **2017**, *7*, 1601424. [[CrossRef](#)]
14. Quan, Y.; Zhang, M.; Wang, G.; Lu, L.; Wang, Z.; Xu, H.; Liu, S.; Min, Q. 3D hierarchical porous CuS flower-dispersed CNT arrays on nickel foam as a binder-free electrode for supercapacitors. *New J. Chem.* **2019**, *43*, 10906–10914. [[CrossRef](#)]
15. Wu, H.; Li, Y.; Li, Q. Facile synthesis of CuS Nanostructured flowers and their visible light photocatalytic properties. *Appl. Phys. A* **2017**, *123*, 196. [[CrossRef](#)]
16. Nabi, G.; Tanveer, M.; Tahir, M.B.; Kiran, M.; Nawaz, T. Mixed solvent based surface modification of CuS nanostructures for an excellent photocatalytic application. *Inorg. Chem. Commun.* **2020**, *121*, 108205. [[CrossRef](#)]
17. Iqbal, S.; Bahadur, A.; Anwer, S.; Shoaib, M.; Liu, G.; Li, H.; Raheel, M.; Javed, M.; Khalid, B. Designing novel morphologies of L-cysteine surface capped 2D covellite (CuS) nanoplates to study the effect of CuS morphologies on dye degradation rate under visible light. *CrystEngComm* **2020**, *22*, 4162–4173. [[CrossRef](#)]
18. Liu, X.; Guo, M.; Wei, C.; Ji, X.; Zheng, W. Purposely synthesis of hierarchical CuS nanoflowers composed of ultrathin nanoflakes with exposed (001) facets using a solvent-template ionic liquid and their application in supercapacitors. *Mater. Sci. Eng. B* **2021**, *273*, 115433. [[CrossRef](#)]
19. Liu, X.; Liu, G.; Wang, L.; Li, Y.; Ma, Y.; Ma, J. Morphology- and facet-controlled synthesis of CuO micro/nanomaterials and analysis of their lithium ion storage properties. *J. Power Sources* **2016**, *312*, 199–206. [[CrossRef](#)]
20. Liu, G.; Liu, X.; Wang, L.; Ma, J.; Xie, H.; Ji, X.; Guo, J.; Zhang, R. Hierarchical  $\text{Li}_4\text{Ti}_5\text{O}_{12}$ - $\text{TiO}_2$  microspheres assembled from nanoflakes with exposed  $\text{Li}_4\text{Ti}_5\text{O}_{12}$  (011) and anatase  $\text{TiO}_2$  (001) facets for high-performance lithium-ion batteries. *Electrochim. Acta* **2016**, *222*, 1103–1111. [[CrossRef](#)]
21. Liu, X.; Chen, H.; Liu, R.; Liu, G.; Ji, X.; Feng, Y.; Ma, J. Ionic liquid-assisted synthesis of hierarchical  $\text{Ti}_2\text{Nb}_{10}\text{O}_{29}$  porous microspheres coated by ultrathin N-doped carbon layers for high-performance lithium-ion battery. *Ceram. Int.* **2021**, *47*, 17606–17641. [[CrossRef](#)]
22. Liu, X.; Fan, H.; Li, B.; Hu, M.; Hu, Y.; Liu, M.; Liu, G.; Ma, J.  $\alpha$ - $\text{Fe}_2\text{O}_3$  hollow microspheres assembled by ultra-thin nanoflakes exposed with (241) high-index facet: Solvothermal synthesis, lithium storage performance, and superparamagnetic property. *Int. J. Hydrogen Energy* **2019**, *44*, 1070–1077. [[CrossRef](#)]
23. Yang, Z.; Shang, Z.; Liu, F.; Chen, Y.; Liu, G.; Chen, Y.; Wang, X.; Zhang, B.; Liu, G. Hollow porous  $\text{BiOCl}$  microspheres assembled with single layer of nanocrystals: Spray solution combustion synthesis and the enhanced photocatalytic properties. *Nanotechnology* **2021**, *32*, 205602. [[CrossRef](#)] [[PubMed](#)]
24. Wang, Y.; Sun, Y.; Zhang, X.; Wen, Y.; Guo, J. Sacrificial template formation of  $\text{CoMoO}_4$  hollow nanostructures constructed by ultrathin nanosheets for robust lithium storage. *RSC Adv.* **2016**, *6*, 51710–51715. [[CrossRef](#)]

25. Zhang, L.; Jiu, H.; Fu, Y.; Sun, Y.; Chen, P.; Li, Y.; Ma, S. Facile synthesis and luminescence of GdPO<sub>4</sub>:Eu hollow microspheres by a sacrificial template route. *Mater. Lett.* **2013**, *101*, 47–50. [[CrossRef](#)]
26. Dai, C.; Tian, X.; Nie, Y.; Tian, C.; Yang, C.; Zhou, Z.; Li, Y.; Gao, X. Successful synthesis of 3D CoSe<sub>2</sub> hollow microspheres with high surface roughness and its excellent performance in catalytic hydrogen evolution reaction. *Chem. Eng. J.* **2017**, *321*, 105–112. [[CrossRef](#)]
27. Cao, S.W.; Zhu, Y.J. Iron oxide hollow spheres: Microwave-hydrothermal ionic liquid preparation, formation mechanism, crystal phase and morphology control and properties. *Acta Mater.* **2009**, *57*, 2154–2165. [[CrossRef](#)]
28. Du, W.; Qian, X.; Ma, X.; Gong, Q.; Cao, H.; Yin, H. Shape-controlled synthesis and self-assembly of hexagonal covellite (CuS) nanoplatelets. *Chem. Eur. J.* **2007**, *13*, 3241–3247. [[CrossRef](#)] [[PubMed](#)]
29. Dong, L.; Tang, Y.; Li, B.; Zhou, L.; Gong, F.; He, H.; Sun, B.; Tang, C.; Gao, F.; Dong, L. Influence of molar ratio and calcination temperature on the properties of Ti<sub>x</sub>Sn<sub>1-x</sub>O<sub>2</sub> supporting copper oxide for CO oxidation. *Appl. Catal. B* **2016**, *180*, 451–462. [[CrossRef](#)]
30. Liang, H.; Shuang, W.; Zhang, Y.; Chao, S.; Han, H.; Wang, X.; Zhang, H.; Yang, L. Graphene-like multilayered CuS nanosheets assembled into flower-like microspheres and their electrocatalytic oxygen evolution properties. *ChemElectroChem* **2018**, *5*, 494–500. [[CrossRef](#)]
31. Hsu, Y.K.; Chen, Y.C.; Lin, Y.G. Synthesis of copper sulfide nanowire arrays for high-performance supercapacitors. *Electrochim. Acta* **2014**, *139*, 401. [[CrossRef](#)]
32. Liu, X.; Duan, X.; Peng, P.; Zheng, W. Hydrothermal synthesis of copper selenides with controllable phases and morphologies from an ionic liquid precursor. *Nanoscale* **2011**, *3*, 5090–5095. [[CrossRef](#)]
33. Shakya, S.; Prakash, G.V. Formation of PbO hexagonal nanosheets and their conversion into luminescent inorganic-organic perovskite nanosheets: Growth and mechanism. *RSC Adv.* **2015**, *5*, 27946–27952. [[CrossRef](#)]
34. Wen, L.L.; Hong, Y.Z.; Jing, L.; Qiang, W.; Yuan, F.L.; Cheng, Z.H. H<sub>2</sub>S bubbles-assisted synthesis of hollow Cu<sub>2-x</sub>Se<sub>y</sub>S<sub>1-y</sub>/reduced graphene oxide nanocomposites with tunable compositions and localized surface plasmon resonance. *RSC Adv.* **2015**, *5*, 91206–91212.
35. Zhan, Q.; Shi, X.; Fan, D.; Zhou, L.; Wei, S. Solvent mixing generating air bubbles as a template for polydopamine nanobowl fabrication: Underlying mechanism, nanomotor assembly and application in cancer treatment. *Chem. Eng. J.* **2021**, *404*, 126443. [[CrossRef](#)]
36. Zhang, S.; Zeng, Y.; Wang, Z.; Zhao, J.; Dong, G. Glycerol-controlled synthesis of MoS<sub>2</sub> hierarchical architectures with well-tailored subunits and enhanced electrochemical performance for lithium ion batteries. *Chem. Eng. J.* **2017**, *4*, 487–496. [[CrossRef](#)]
37. Wang, Z.; Zhang, X.; Zhang, Y.; Li, M.; Qin, C.; Bakenov, Z. Chemical dealloying synthesis of CuS nanowire-on-nanoplate network as anode materials for Li-ion batteries. *Metals* **2018**, *8*, 252. [[CrossRef](#)]
38. Ren, C.; Yue, H.; Wang, G.; Wen, Q.; Jin, R. Copper sulfides nanocrystals encapsulated in polypyrrole nanotubes for stable lithium storage. *Mater. Lett.* **2021**, *282*, 128840. [[CrossRef](#)]
39. Zhang, B.; Gao, X.W.; Wang, J.Z.; Chou, S.L.; Konstantinov, K.; Liu, H.K. CuS nanoflakes, microspheres, microflowers, and nanowires: Synthesis and lithium storage properties. *J. Nanosci. Nanotechnol.* **2013**, *13*, 1309–1316. [[CrossRef](#)]
40. Hosseinpour, Z.; Scarpellini, A.; Najafshirtari, S.; Marras, S.; Colombo, M.; Alemi, A.; Volder, M.D.; George, C.; Lesnyak, V. Morphology-dependent electrochemical properties of CuS hierarchical superstructures. *ChemPhysChem* **2015**, *16*, 3418–3424. [[CrossRef](#)]
41. Han, Y.; Wang, Y.; Gao, W.; Wang, Y.; Jiao, L.; Yuan, H.; Liu, S. Synthesis of novel CuS with hierarchical structures and its application in lithium-ion batteries. *Powder Technol.* **2011**, *212*, 64–68. [[CrossRef](#)]
42. Zhang, Y.; Li, K.; Wang, Y.; Zeng, J.; Ji, P.; Zhao, J. Copper sulfide microspheres wrapped with reduced graphene oxide for high-capacity lithium-ion storage. *Mater. Sci. Eng. B* **2016**, *213*, 57–62. [[CrossRef](#)]
43. Fu, Y.; Manthiram, A. Electrochemical properties of Cu<sub>2</sub>S with ether-based electrolyte in Li-ion batteries. *Electrochim. Acta* **2013**, *109*, 716–719. [[CrossRef](#)]
44. Han, F.; Li, W.C.; Li, D.; Lu, A.H. In situ electrochemical generation of mesostructured Cu<sub>2</sub>S/C composite for enhanced lithium storage: Mechanism and material properties. *ChemElectroChem* **2014**, *1*, 733–740. [[CrossRef](#)]
45. Jia, C.; Zhang, X.; Yang, P. Anatase/rutile-TiO<sub>2</sub> hollow hierarchical architecture modified by SnO<sub>2</sub> toward efficient lithium storage. *Int. J. Hydrogen Energy* **2018**, *43*, 2237–2246. [[CrossRef](#)]
46. Guo, Y.; Li, S.; Fang, Q.; Zuo, J.; Liu, M.; Zhang, J. An integrated electrode based on nanoflakes of MoS<sub>2</sub> on carbon cloth for enhanced lithium storage. *RSC Adv.* **2020**, *10*, 9335–9340. [[CrossRef](#)] [[PubMed](#)]
47. Li, H.; Wang, Y.; Huang, J.; Zhang, Y.; Zhao, J. Microwave-assisted synthesis of CuS/graphene composite for enhanced lithium storage properties. *Electrochim. Acta* **2017**, *225*, 443–451. [[CrossRef](#)]
48. Zhou, H.; Guo, J.; Fang, N.; Liang, J.; Shen, T.; Yuan, S. Investigation of photocatalytic performance of CuS/Bi<sub>2</sub>WO<sub>6</sub> and degradation pathway of RhB in water. *J. Water Supply Res. T.* **2020**, *69*, 145–149. [[CrossRef](#)]
49. Zhang, Y.; Zhang, B.; Ge, Z.; Zhu, L.; Li, Y. Preparation by solvothermal synthesis, growth mechanism, and photocatalytic performance of CuS nanopowders. *Eur. J. Inorg. Chem.* **2014**, *14*, 2368–2375. [[CrossRef](#)]
50. Deng, X.; Wang, C.; Yang, H.; Shao, M.; Zhang, S.; Wang, X.; Ding, M.; Huang, J.; Xu, X. One-pot hydrothermal synthesis of CdS decorated CuS microflower-like structures for enhanced photocatalytic properties. *Sci. Rep.* **2018**, *7*, 3877. [[CrossRef](#)]

51. Seo, K.; Sinha, K.; Novitskaya, E.; Graeve, O.A. Polyvinylpyrrolidone (PVP) effects on iron oxide nanoparticle formation. *Mater. Lett.* **2018**, *25*, 203–206. [[CrossRef](#)]
52. Chen, P.; Su, Y.; Liu, H.; Wang, Y. Interconnected tin disulfide nanosheets grown on graphene for Li-ion storage and photocatalytic applications. *ACS Appl. Mater. Interfaces* **2013**, *5*, 12073–12082. [[CrossRef](#)] [[PubMed](#)]
53. Zhang, K.; Jin, L.; Yang, Y.; Guo, K.; Hu, F. Novel method of constructing CdS/ZnS heterojunction for high performance and stable photocatalytic activity. *J. Photochem. Photobiol. A* **2019**, *380*, 11859. [[CrossRef](#)]
54. Zhong, W.; Wu, X.; Wang, P.; Fan, J.; Yu, H. Homojunction CdS photocatalysts with a massive S<sub>2</sub>-adsorbed surface phase: One-step facile synthesis and high H<sub>2</sub>-evolution performance. *ACS Sustain. Chem. Eng.* **2020**, *8*, 543–551. [[CrossRef](#)]
55. Yepsen, O.; Yáñez, J.; Mansilla, H.D. Photocorrosion of copper sulfides: Toward a solar mining industry. *Sol. Energy* **2018**, *171*, 106–111. [[CrossRef](#)]
56. Hou, L.; Niu, Y.; Yang, F.; Ge, F.; Yuan, C. Facile solvothermal synthesis of hollow biobr submicrospheres with enhanced visible-light-responsive photocatalytic performance. *J. Anal. Methods Chem.* **2020**, *2020*, 3058621. [[CrossRef](#)] [[PubMed](#)]
57. Liu, Y.; Huang, C.; Zhou, T.; Hu, J. Morphology-preserved transformation of CdS hollow structures toward photocatalytic H<sub>2</sub> evolution. *CrystEngComm* **2020**, *22*, 1057–1062. [[CrossRef](#)]
58. Nguyen, C.C.; Vu, N.N.; Do, T.O. Recent advances in the development of sunlight-driven hollow structure photocatalysts and their applications. *J. Mater. Chem. A* **2015**, *3*, 18345–18359. [[CrossRef](#)]
59. Li, C.X.; Han, L.J.; Liu, R.J.; Li, H.H.; Zhang, S.J.; Zhang, G.J. Controlled synthesis of CdS micro/nano leaves with (0001) facets exposed: Enhanced photocatalytic activity toward hydrogen evolution. *J. Mater. Chem.* **2012**, *22*, 23815–23820. [[CrossRef](#)]
60. Hao, X.; Hu, Y.; Cui, Z.; Zhou, J.; Wang, Y.; Zou, Z. Self-constructed facet junctions on hexagonal CdS single crystals with high photoactivity and photostability for water splitting. *Appl. Catal. B-Environ.* **2019**, *244*, 694–703. [[CrossRef](#)]
61. Li, Y.; Tang, Z.; Zhang, J.; Zhang, Z. Exposed facet and crystal phase tuning of hierarchical tungsten oxide nanostructures and their enhanced visible-light-driven photocatalytic performance. *CrystEngComm* **2015**, *17*, 9102–9911. [[CrossRef](#)]

**Disclaimer/Publisher's Note:** The statements, opinions and data contained in all publications are solely those of the individual author(s) and contributor(s) and not of MDPI and/or the editor(s). MDPI and/or the editor(s) disclaim responsibility for any injury to people or property resulting from any ideas, methods, instructions or products referred to in the content.